Electronic Supplementary Material (ESI) for Physical Chemistry Chemical Physics.

Supplementary Information

Identifying major transient species by combining time-resolved X-ray solution scattering and X-ray absorption spectroscopy

Kyung Hwan Kim, Jeongho Kim, Key Young Oang, Jae Hyuk Lee, Daniel Grolimund, Christopher J. Milne, Thomas J. Penfold, Steven L. Johnson, Andreas Galler, Tae Wu Kim, Jong Goo Kim, Deokbeom Suh, Jiwon Moon, Joonghan Kim, Kiryong Hong, Laurent Guérin, Tae Kyu Kim, Michael Wulff, Christian Bressler, and Hyotcherl Ihee*

Experimental setup for TRXL data collection

Time-resolved X-ray solution scattering measurement was performed at the ID09B beamline of the European Synchrotron Radiation Facility (ESRF). The 16-bunch mode of ESRF was used for the measurement so that single X-ray pulses can be isolated from the storage ring by the chopper. The X-rays were delivered by the U71 undulator with a spectrum peaked at 18 keV. The spectrum has a long wavelength tail with the bandwidth of ~3 % FWHM. The full spectrum was used without being monochromatized. The blurring effect to the scattering curve due to the polychromaticity was not substantial and properly corrected by the polychromatic correction. Single X-ray pulses were isolated by a high-speed chopper that has a triangular-shaped rotor with a tunnel spinning at ~986.3 kHz, a subharmonic of the orbit frequency of the synchrotron. A 150-fs laser pulse (at 800 nm) was converted to the third harmonic (267 nm) and stretched to 2 ps by transmission through a fused silica rod of 30 cm length to avoid multiphoton effects. The laser pulses were synchronized with the X-ray pulses at a repetition rate of 986.3 Hz. The laser pulse of ~60 μJ energy was focused to a spot of 0.15 × 0.15 mm^2 size at the sample position, yielding a fluence of ~2.6 mJ/mm^2. A solution of iodoform in methanol at the concentration of 1 – 20 mM was circulated through a sapphire nozzle with 300 μm aperture and excited by the laser pulse. The X-ray pulse was used to probe the progress of the reaction induced by the photoexcitation at well-defined laser–X-ray time delays. Note that the time delay is defined by the time difference between the centers of the two pulses. The scattering patterns were recorded by a CCD detector as a function of the time delay. The laser-off images were acquired with the X-ray pulse arriving 5 ns earlier than the laser pulse in order to eliminate the contribution of the (unexcited) ground state. These laser-off images were used as a reference for calculating the time-resolved difference X-ray scattering patterns. A laser-off image was collected per every 3 or 4 laser-on images to compensate for slow drifts of the X-ray intensity in the beamline. To follow the early events occurring within the time resolution (~100 ps), the time-slicing scheme was employed as described in Figure S1. According to this scheme, the difference scattering curve measured at –20 ps contains the information about the chemical process occurring between 0 and ~30 ps. The scattering curves were measured at the following time delays: –5 ns, –200 ps, –100 ps, –20 ps, 0 ps, 50 ps, 100 ps, 150 ps, 300 ps. To attain high signal-

to-noise ratio enough for accurate data analysis, more than 50 images were acquired and averaged at each time delay.

Experimental setup for TR-XAS data collection

Time-resolved X-ray absorption spectroscopy measurement was performed at the microXAS beamline of the Swiss Light Source (SLS) at the Paul Scherrer Institute. A 60 mM solution of iodoform dissolved in methanol was circulated through a sapphire nozzle with 200 μm aperture. A ~100 fs laser pulse (at 800 nm) was converted to the third harmonic (267 nm) for the excitation of the sample solution. Here we note that the temporal widths of the laser pulses used for the TRXL (2 ps) and TR-XAS (150 fs) experiments were different from each other. However, since it is known that the two-photon excitation does not occur even with the excitation using 150-fs pulses,[1] there should be no difference in the reaction dynamics depending on the laser pulse width. The laser pulse of ~ 40 μJ energy was focused to a spot of 0.12 × 0.12 mm^2 size at the sample position, yielding the fluence of ~2.7 mJ/mm^2. Monochromatic and tunable hard X-ray pulse of ~100 ps duration was used to probe the progress of the reaction as a function of well-defined time delay between the laser and X-ray pulses. The measurement was performed at two different absorption edges (L_1 and L_3 edges) of iodine atom. Difference XANES spectra were measured by changing the X-ray energy around the absorption edge at fixed time delays: 100ps, 300 ps and 1ns for L_1 edge and 100 ps and 2 ns for L_3 edge (also measured at other intermediate time delays but not shown here). In addition, by changing the time delay between the X-ray and laser pulses, the time-dependent amplitude change of the difference spectra was measured at two fixed X-ray energies: 5.1857 keV for L_1 edge and 4.5623 keV for L_3 edge.

Computational details of DFT calculations

All molecular structures were optimized using a density functional theory (DFT) method. Subsequent harmonic vibrational frequency calculations were also performed on the optimized molecular structures. We used the recently-developed ωB97X functional[2] as DFT exchange-correlation functional. From a recent DFT study by our group, it was found that the ωB97X can

accurately predict the molecular structures of halomethanes and haloethanes, especially the C–I distance.[3] To treat the scalar relativistic effect of iodine, we used aug-cc-pVTZ-PP small-core relativistic effective core potential (RECP).[4] For other atoms (C and H), aug-cc-pVTZ all-electron basis sets were used. We also used the integral-equation-formalism polarizable continuum model (IEFPCM) method[5] to describe solvent effect implicitly. For the calculation of $CH_2I{-}I$ isomer, we used the broken-symmetry method to consider biradical character of the isomer. All DFT calculations were performed using the Gaussian09 program.[6]

We note that, in the present work, we improved the level of the DFT calculation compared with our previous TRXL study on CHI_3,[7] where the B3LYP functional was used. According to our recent DFT study,[3] the B3LYP functional tend to overestimate the C–I distance in contrast the ωB97X functional used in the present work. As a result, the optimized structure of the isomer species used in this work (I–I distance: 3.174 Å, C–I–I angle: 113º) is slightly different from the one used in our previous study (I–I distance: 3.30 Å, C–I–I angle: 134º).[7] In order to examine the effect of the changes in the isomer structure on the conclusion of the present work, we calculated theoretical scattering curves using various possible structures of the isomer with the C–I–I angle varied from 133° to 93° and the I–I distance varied from 3.674 to 2.674 Å. As can be seen in Figure S3, none of them fit our experimental data as well as the best fit in Fig. 2b. On the other hand, the C–I distance of the radical species used in this work (C–I distance: 2.044 Å) is almost the same as the one used in our previous study (C–I distance: 2.07 Å). Therefore, the good fits for the radical pathway in both the present work and our previous study are still valid.

We calculated Raman intensity of $CHI_2{-}I$, CH_2I, and CH_2I^+ using ωB97X/aug-cc-pVTZ to compare with the Raman experiment.[1, 8-9] The conventional DFT method, B3LYP/def2-TZVP, was also used for the comparison. The calculated results are summarized in Tables S2 and S3. The time-dependent DFT (TDDFT) method was used to characterize the excited states of $CHI_2{-}I$, CH_2I, and CH_2I^+. In the broken-symmetry calculations for the isomer, only excited states whose $\langle S^2 \rangle$ value is less than 1.000 were listed. The results of TDDFT are summarized in Tables S2 and S3.

Molecular dynamics simulation

To estimate the solute-solvent cage contribution to the difference scattering signal, we performed the molecular dynamics (MD) simulation for all the chemical species involved in the reaction. All the MD simulations were performed by following the protocols described in our previous publications[10-11] using the program MOLDY.[12] The periodic boundary conditions were used with a cubic box of 32.6 Å size containing one solute molecule embedded in 512 methanol molecules. This condition satisfies the density of methanol at standard temperature and pressure. The molecules were kept rigid during the simulation. For the description of methanol solvent, we used the H1 model.[13] The charges on individual atoms were obtained by DFT calculation and were kept fixed during the simulation. The radial distribution functions (RDFs) were calculated up to 20 Å with 0.02 Å steps and used for the calculation of the scattering intensity. The contributions from the solute only, solute-solvent cage, and solvent are shown in Fig S2.

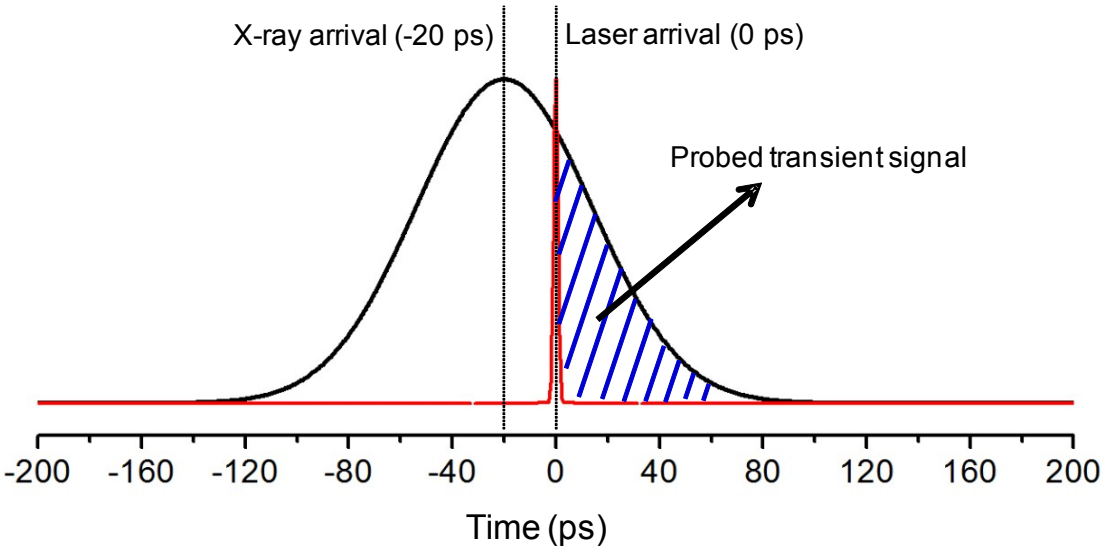

Figure S1. Concept of the laser-time-slicing technique. When the time delay between the short laser and the longer X-ray pulse is smaller than the width of the X-ray pulse, only part of the temporal profile of X-ray pulse contributes to the transient signal, effectively improving the time resolution of the measurement. For example, the difference scattering curve measured at –20 ps time delay contains the information on the chemical process occurring between 0 and ~30 ps.

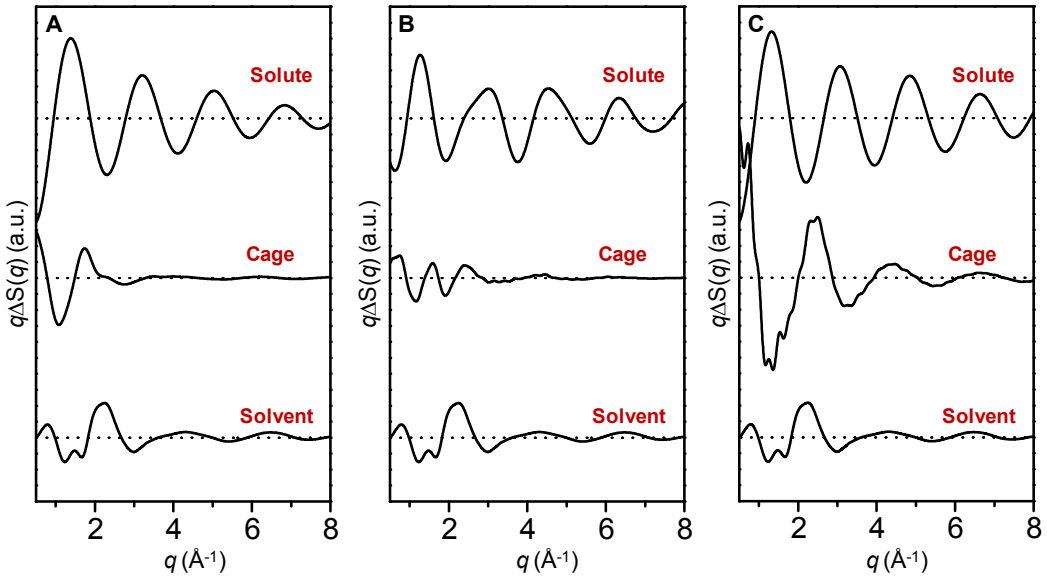

Figure S2. Contributions from the solute only, solute-solvent cage, and solvent thermal heating to the theoretical difference scattering curves for three different reaction pathways shown in Fig. 2, (A) dissociation into CHI_2 radical and I, (B) CHI_2–I isomer formation, and (C) dissociation into CHI_2^+ and I^- ions. The solute contribution was calculated by the Debye formula using DFT-optimized molecular structures of all the chemical species and their time-dependent concentrations determined from the fitting to the experimental difference scattering curves. The solute-solvent cage term was calculated from the radial distribution functions of solute-solvent atomic pairs obtained from the MD simulation. The solvent heating signal was obtained from a separate IR-heating experiment.[14] We note that the $CHI_2^+ + I^-$ pathway exhibits much larger cage term, especially in a low q-region, than the $CHI_2 + I$ pathway. As a result, as is seen in Fig. 2, the theoretical scattering curves for the two pathways are very different from each other, especially in the low q-region.

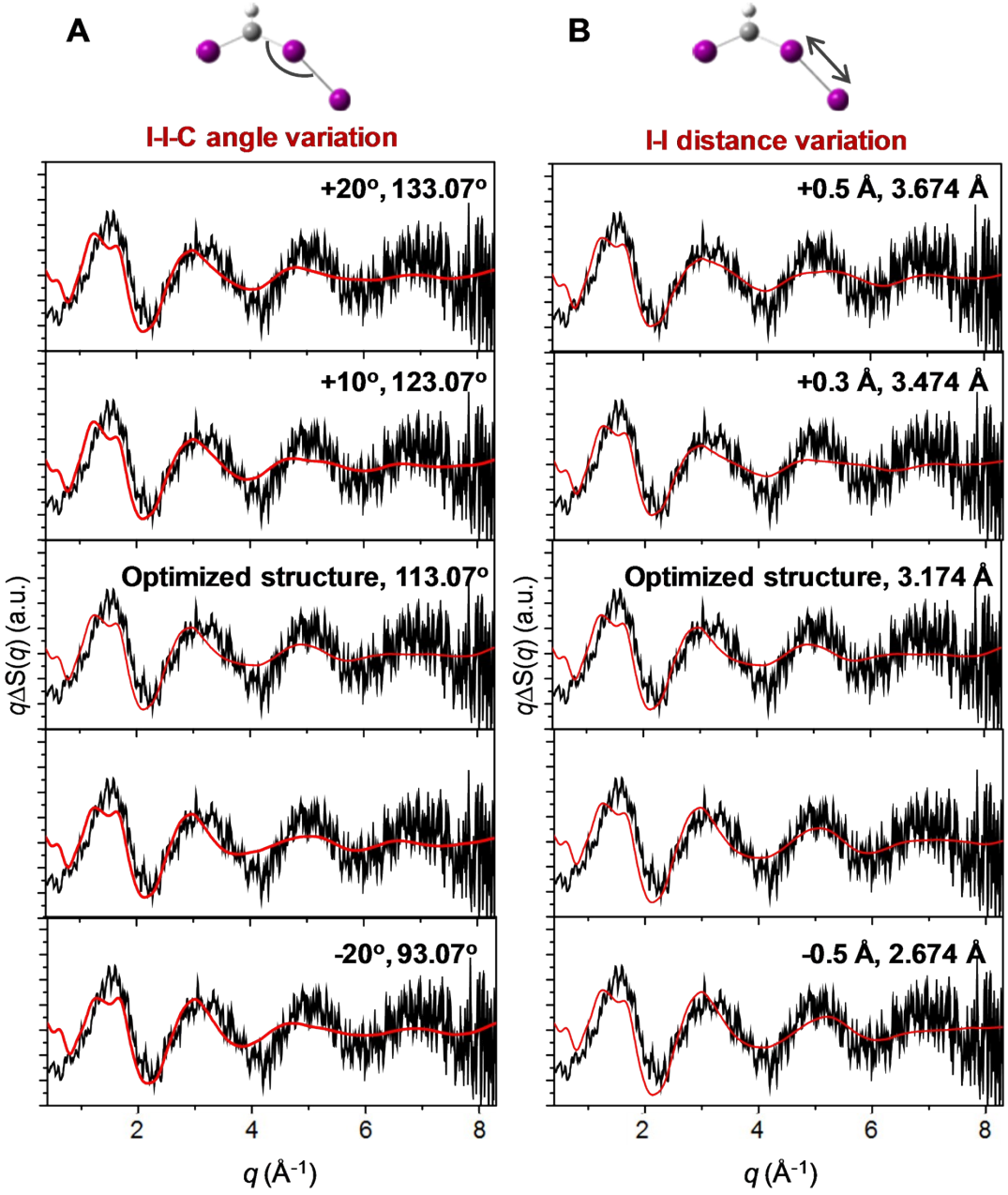

Figure S3. Theoretical calculation of difference scattering curves at –20 ps time delay for various isomer structures.

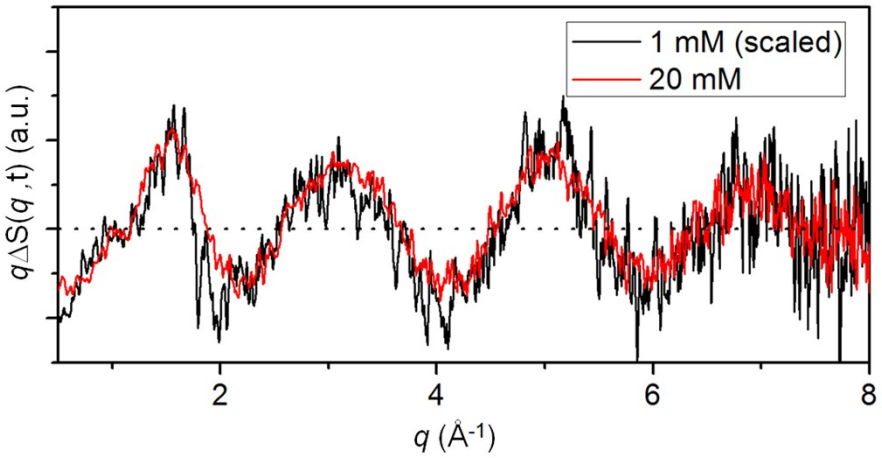

Figure S4. Difference scattering curves at 100 ps time delay for a diluted sample (1 mM, black) and a concentrated sample (20 mM, red) are compared. The scattering curve for the diluted sample was scaled up to match the curve for the concentrated sample to ease the comparison.

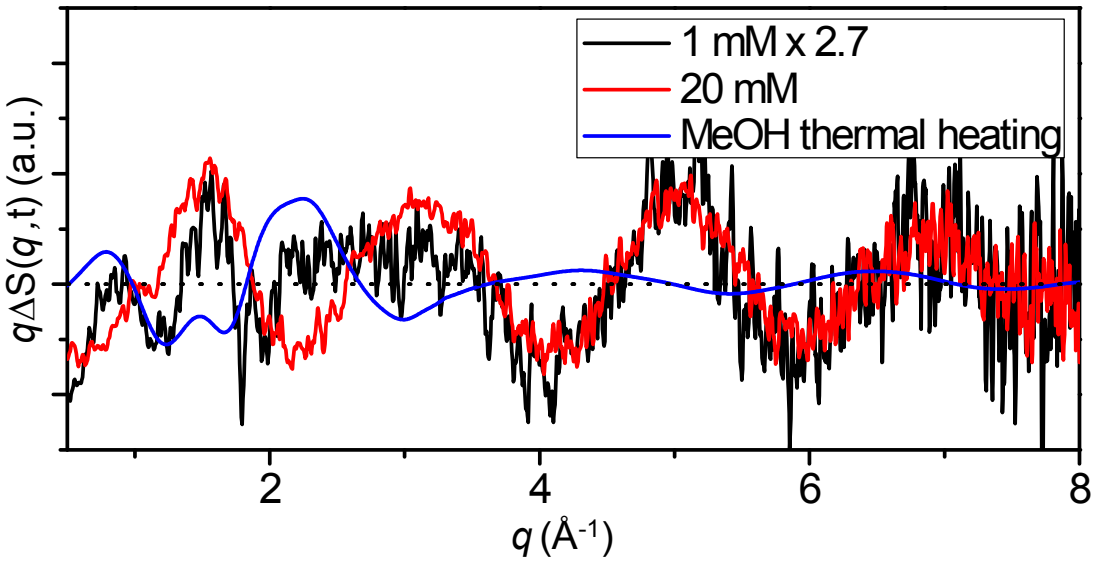

Figure S5. Strategy of scaling the scattering curve for the diluted (1 mM) sample with respect to the one for the concentrated sample. With the linear scaling of the difference scattering curve for the diluted sample (black curve, multiplied by 2.7), we were not able to achieve a perfect agreement with the curve for the 20-mM sample (red), especially in the low q range. This discrepancy between the two data is attributed to the difference in the amount of heat released to the solvent in the solutions of the two different concentrations. Accordingly, the difference between the two curves corresponds to the thermal heating signal of methanol (blue). To resolve this issue, we subtracted the solvent heating signal from the 1-mM curve to obtain the scattering curve shown in Figure S4.

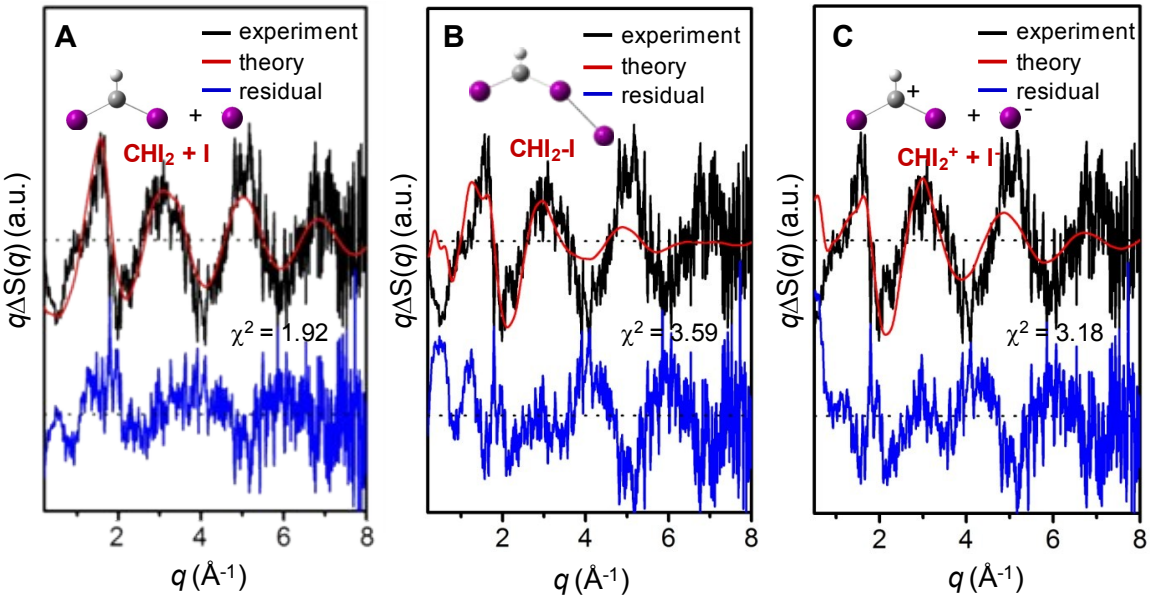

Figure S6. Theoretical calculation of the difference scattering curve at 100 ps time delay for the diluted sample (1 mM). The experimental curve (black) was fit by theoretical curves (red) calculated by considering three different candidate reaction pathways: (A) dissociation into CHI_2 radical and I, (B) CHI_2–I isomer formation and (C) dissociation into CHI_2^+ and I^- ions. The residuals (blue) displayed at the bottom represent the difference between the experimental and theoretical curves. The CHI_2 radical channel fits the experimental curve much better than the other channels, giving substantially smaller χ^2 values.

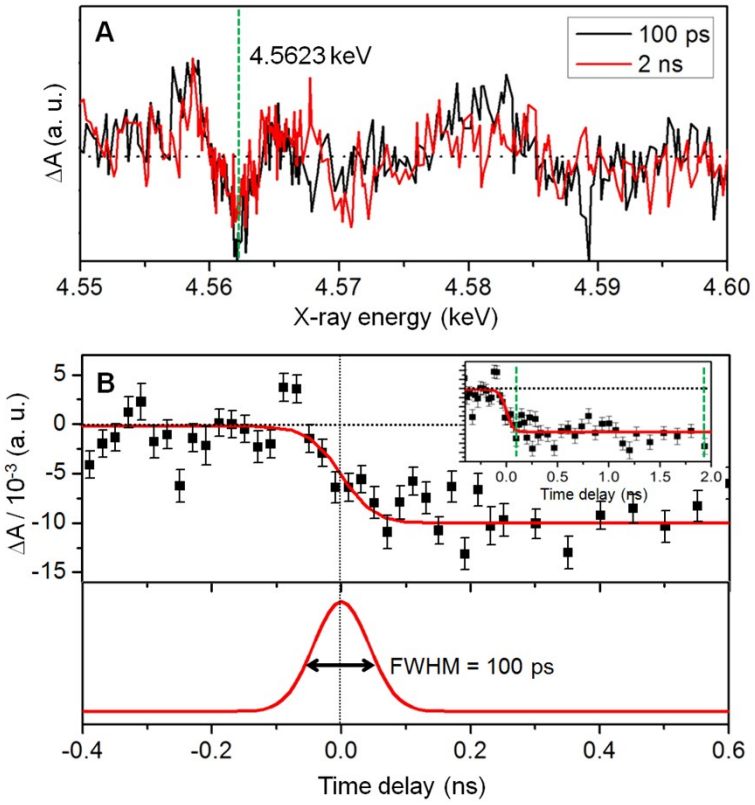

Figure S7. Time-resolved XANES measurement of iodoform photolysis at the L_3 edge of the iodine atom. (A) Difference XANES spectra measured at the time delays of 100 ps and 2 ns are overlaid. (B) Temporal amplitude change of the difference absorption spectra at a peak position (E = 4.5623 keV) marked with a green dashed line in Figure 4A is displayed from –0.4 to 0.6 ns. The time trace in this time range is well described by a single error function of 100 ps FWHM (red). Inset shows the time trace in a longer time range up to 2 ns.

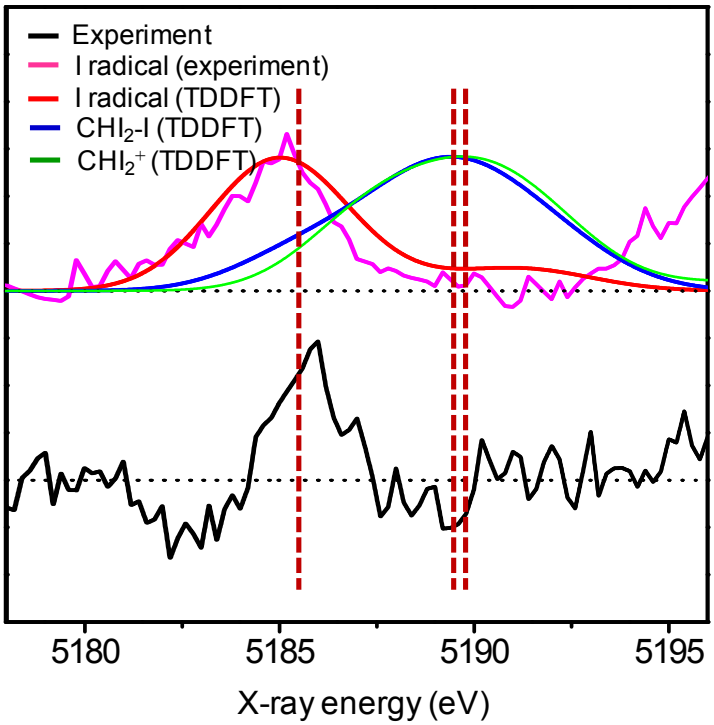

Figure S8. Theoretical absorption spectra of the 2s → 5p transition simulated using time-dependent density functional theory, within the approximation of the BP86 exchange and correlation functional as implemented within ORCA.[9] A triple zeta valence with polarization functions (TZVP) basis set was used for all of the atoms. To incorporate the solvation effect, 100 different MD configurations with 30 surrounding solvent molecules were used. The energy axis was calibrated in comparison with the experimental static XANES spectrum of the I radical.[15] It can be seen that the absorption peak of the I radical is located at the same energy (5.1857 keV) as the main positive peak in our experimental difference absorption spectrum.

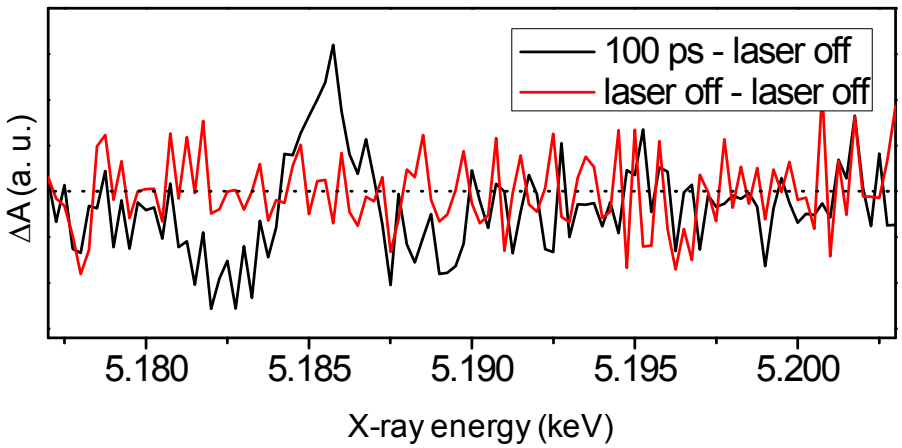

Figure S9. The difference XANES spectrum obtained by taking the difference between two independent static spectra measured with laser off is compared with the difference spectrum measured at 100 ps time delay. It can be clearly seen that the laser-off difference spectrum has no meaningful feature.

Table S1. The calculated XYZ coordinates of all the chemical species involved in the reaction.

		X	Y	Z
CHI_3	**C**	0.000000	0.000000	0.563090
	H	0.000000	0.000000	1.644118
	I	0.000000	2.048420	-0.031589
	I	1.773984	-1.024210	-0.031589
	I	-1.773984	-1.024210	-0.031589
CHI_2	**C**	-0.001118	0.897229	0.000000
	H	0.125174	1.967656	0.000000
	I	-0.001118	-0.069349	1.801431
	I	-0.001118	-0.069349	-1.801431
CHI_2I	**C**	1.408030	0.657117	0.800078
	H	1.493438	0.810614	1.864947
	I	-0.252015	1.327456	-0.085275
	I	2.708623	-0.661378	-0.057658
	I	-2.644186	-0.755763	0.017170
CHI_2^+	**C**	0.000000	0.820172	0.000000
	H	0.000012	1.904325	0.000000
	I	0.000000	-0.064390	1.769238
	I	0.000000	-0.064390	-1.769238

Table S2. Excited states energies (nm) with oscillator strengths in brackets.

			Excited State 1	Excited State 2	Excited State 3	Excited State 4	Excited State 5	Excited State 6
Methanol	ωB97X/aug-cc-pVTZ	CHI_2–I	606.8 (0.2750)	357.6 (0.2172)	289.1 (0.0523)	271.0 (0.0511)	243.5 (0.0252)	
		CHI_2	449.1 (0.0001)	309.0 (0.0002)	288.7 (0.0004)	246.2 (0.0357)	239.0 (0.0171)	229.7 (0.0008)
		CHI_2^+	486.0 (0.0000)	440.5 (0.0003)	351.6 (0.2831)	235.8 (0.0352)	234.2 (0.0000)	227.4 (0.0197)
Acetonitrile	ωB97X/aug-cc-pVTZ	CHI_2–I	608.9 (0.2774)	357.9 (0.2179)	289.3 (0.0532)	271.1 (0.0513)	243.5 (0.0254)	
		CHI_2	449.1 (0.0001)	309.0 (0.0002)	288.7 (0.0004)	246.2 (0.0360)	239.0 (0.0173)	229.7 (0.0008)
		CHI_2^+	485.9 (0.0000)	440.5 (0.0003)	352.0 (0.2852)	235.8 (0.0353)	234.2 (0.0000)	227.5 (0.0199)
Cyclohexane	ωB97X/aug-cc-pVTZ	CHI_2–I	535.5 (0.2793)	355.6 (0.2034)	275.8 (0.0544)	269.9 (0.0266)	246.0 (0.0262)	232.4 (0.0005)
		CHI_2	454.4 (0.0001)	311.3 (0.0002)	290.6 (0.0004)	248.5 (0.0388)	240.8 (0.0180)	232.0 (0.0010)
		CHI_2^+	495.9 (0.0000)	447.3 (0.0004)	356.0 (0.2927)	237.0 (0.036)	234.9 (0.0000)	228.0 (0.0198)

Table S3. Resonance Raman frequencies (cm^{-1}). Intensity in brackets.

			ν_1	ν_2	ν_3	ν_4	ν_5	ν_6	ν_7	ν_8	ν_9
Methanol	ωB97X/aug-cc-pVTZ	CHI_2–I	20.65 (99.49)	100.31 (1812.10)	119.01 (127.09)	142.03 (518.98)	469.15 (11458.95)	538.63 (1803.52)	757.47 (5394.71)	1169.59 (1173.21)	3254.87 (5735.44)
		CHI_2	131.00 (2.94)	164.88 (6.05)	519.05 (14.13)	745.85 (0.21)	1128.87 (0.62)	3265.67 (239.85)			
		CHI_2^+	150.91 (12.23)	570.89 (25.76)	738.44 (1.15)	808.19 (0.08)	1218.69 (1.59)	3219.85 (154.91)			
	B3LYP/def2-TZVP	CHI_2–I	81.62 (52.38)	135.62 (57.67)	187.31 (21.78)	502.96 (530.25)	663.13 (452.75)	749.58 (870.20)			
		CHI_2	160.29 (20.93)	385.10 (64.19)	512.39 (35.89)	652.59 (3.21)					
		CHI_2^+	151.10 (23.45)	544.55 (22.31)	733.38 (0.64)	774.21 (4.11)					
Acetonitrile	ωB97X/aug-cc-pVTZ	CHI_2–I	20.65 (101.32)	100.38 (1868.97)	119.03 (130.31)	142.05 (534.41)	469.30 (11781.34)	538.70 (1821.25)	757.52 (5507.12)	1169.72 (1200.21)	3254.88 (5870.04)
		CHI_2	131.00 (2.94)	165.00 (6.10)	519.05 (14 .22)	745.83 (0.22)	1128.88 (0.62)	3265.66 (241.22)			
		CHI_2^+	150.97 (14.99)	570.78 (18.11)	738.41 (1.16)	808.06 (0.40)	1218.68 (14.24)	3219.95 (156.04)			
	B3LYP/def2-TZVP	CHI_2–I	67.99 (28.43)	160.77 (17.88)	288.89 (44.05)	665.34 (487.41)	762.82 (740.47)				
		CHI_2	66.21 (27.41)	382.19 (71.04)	549.33 (21.18)	672.23 (3.51)					
		CHI_2^+	185.26 (24.00)	535.04 (22.10)	728.63 (0.53)	779.92 (4.09)					
Cylohexane	ωB97X/aug-cc-pVTZ	CHI_2–I	19.07 (18.60)	89.93 (68.13)	111.02 (15.85)	140.27 (20.74)	448.23 (566.17)	535.01 (339.96)	752.14 (581.07)	1159.80 (134.32)	3251.62 (617.29)
		CHI_2	130.88 (2.29)	154.88 (2.58)	519.48 (7.89)	749.40 (0.02)	1131.25 (0.13)	3265.50 (125.60)			
		CHI_2^+	151.03 (6.68)	575.22 (17.91)	736.42 (0.64)	82.06 (0.15)	1213.37 (0.01)	3207.85 (89.30)			
	B3LYP/def2-TZVP	CHI_2–I	139.53 (51.68)	173.71 (12.51)	196.53 (4.90)	474.35 (43.90)	657.09 (49.16)	737.72 (192.74)			
		CHI_2	378.39 (26.95)	547.71 (10.422)	675.43 (2.44)						
		CHI_2^+	152.92 (11.92)	542.56 (13.25)	725.70 (0.07)	790.2 (3.49)					

References

1. P. Z. El-Khoury, W. M. Kwok, X. Guan, C. Ma, D. L. Phillips and A. N. Tarnovsky, *ChemPhysChem*, 2009, **10**, 1895-1900.
2. J. D. Chai and M. Head-Gordon, *J. Chem. Phys.*, 2008, **128**.
3. J. Kim, T. K. Kim and H. Ihee, *J. Phys. Chem. A*, 2011, **115**, 1264-1271.
4. K. A. Peterson, B. C. Shepler, D. Figgen and H. Stoll, *J. Phys. Chem. A*, 2006, **110**, 13877-13883.
5. E. Cances, B. Mennucci and J. Tomasi, *J. Chem. Phys.*, 1997, **107**, 3032-3041.
6. M. J. Frisch, G. W. Trucks, H. B. Schlegel, G. E. Scuseria, M. A. Robb, J. R. Cheeseman, G. Scalmani, V. Barone, B. Mennucci, G. A. Petersson, H. Nakatsuji, M. Caricato, H. P. H. X. Li, A. F. Izmaylov, J. Bloino, G. Zheng, J. L. Sonnenberg, M. Hada, M. Ehara, K. Toyota, R. Fukuda, J. Hasegawa, M. Ishida, T. Nakajima, Y. Honda, O. Kitao, H. Nakai, T. Vreven, J. A. Montgomery, J. E. P. Jr., F. Ogliaro, M. Bearpark, J. J. Heyd, E. Brothers, K. N. Kudin, V. N. Staroverov, R. Kobayashi, J. Normand, K. Raghavachari, A. Rendell, J. C. Burant, S. S. Iyengar, M. C. J. Tomasi, J. M. M. N. Rega, M. Klene, J. E. Knox, J. B. Cross, V. Bakken, C. Adamo, J. Jaramillo, R. Gomperts, R. E. Stratmann, O. Yazyev, A. J. Austin, R. Cammi, C. Pomelli, J. W. Ochterski, R. L. Martin, K. Morokuma, V. G. Zakrzewski, G. A. Voth, P. Salvador, J. J. Dannenberg, S. Dapprich, A. D. Daniels, Ö. Farkas, J. B. Foresman, J. V. Ortiz, J. Cioslowski and D. J. Fox, *Gaussian 09*, (2009) Gaussian, Inc., Wallingford CT.
7. J. H. Lee, J. Kim, M. Cammarata, Q. Kong, K. H. Kim, J. Choi, T. K. Kim, M. Wulff and H. Ihee, *Angew. Chem. Int. Ed.*, 2008, **47**, 1047-1050.
8. X. M. Zheng and D. L. Phillips, *Chemical Physics Letters*, 2000, **324**, 175-182.
9. Y. L. Li, D. M. Chen, D. Q. Wang and D. L. Phillips, *Journal of Organic Chemistry*, 2002, **67**, 4228-4235.
10. H. Ihee, M. Lorenc, T. K. Kim, Q. Y. Kong, M. Cammarata, J. H. Lee, S. Bratos and M. Wulff, *Science*, 2005, **309**, 1223-1227.
11. J. H. Lee, M. Wulff, S. Bratos, J. Petersen, L. Guerin, J. C. Leicknam, M. Carnmarata, Q. Kong, J. Kim, K. B. Moller and H. Ihee, *J. Am. Chem. Soc.*, 2013, **135**, 3255-3261.
12. K. Refson, *Comp. Phys. Comm.*, 2000, **126**, 310-329.
13. M. Haughney, M. Ferrario and I. R. Mcdonald, *J. Phys. Chem.*, 1987, **91**, 4934-4940.
14. M. Cammarata, M. Lorenc, T. K. Kim, J. H. Lee, Q. Y. Kong, E. Pontecorvo, M. Lo Russo, G. Schiro, A. Cupane, M. Wulff and H. Ihee, *J. Chem. Phys.*, 2006, **124**, 124504.
15. V. T. Pham, T. J. Penfold, R. M. van der Veen, F. Lima, A. El Nahhas, S. L. Johnson, P. Beaud, R. Abela, C. Bressler, I. Tavernelli, C. J. Milne and M. Chergui, *J. Am. Chem. Soc.*, 2011, **133**, 12740-12748.